European Journal of Environmental and Civil Engineering

Volume 29 Numbers 4 March 2025

Taylor & Francis

ISSN: (Print) (Online) Journal homepage: www.tandfonline.com/journals/tece20

Enhancement of cement mortar's resistance to hydrochloric acid using hybrid SST/DHST fibers and silica fume

Zehra Funda Akbulut

To cite this article: Zehra Funda Akbulut (28 Feb 2025): Enhancement of cement mortar's resistance to hydrochloric acid using hybrid SST/DHST fibers and silica fume, European Journal of Environmental and Civil Engineering, DOI: 10.1080/19648189.2025.2472054

To link to this article: https://doi.org/10.1080/19648189.2025.2472054

Published online: 28 Feb 2025.

Submit your article to this journal

View related articles

View Crossmark data

Full Terms & Conditions of access and use can be found at
https://www.tandfonline.com/action/journalInformation?journalCode=tece20

EUROPEAN JOURNAL OF ENVIRONMENTAL AND CIVIL ENGINEERING
https://doi.org/10.1080/19648189.2025.2472054

Taylor & Francis
Taylor & Francis Group

Check for updates

Enhancement of cement mortar's resistance to hydrochloric acid using hybrid SST/DHST fibers and silica fume

Zehra Funda Akbulut

Department of Mining Engineering, Faculty of Engineering, University of Van Yüzüncü Yıl, Van, Turkey

ABSTRACT

This study investigates the durability of cement mortars against hydrochloric (HCl) acid attacks by incorporating silica fume (SF), melt-extracted straight stainless steel (SST), and double-hooked steel (DHST) fibers. The addition of SF increased the mortar viscosity, reducing workability but significantly improving mechanical strength and resistance to HCl degradation. Combining SF with hybrid SST/DHST fibers showed promising results, demonstrating synergistic effects. SF's pozzolanic activity promoted the formation of calcium-silicate-hydrate (C-S-H) bonds, filling pores, reducing permeability, and enhancing the mortar's resistance to HCl exposure. Furthermore, hybrid SST/DHST fibers outperformed DHST fibers alone in mitigating micro and macro crack formation. Their combined ability to bridge and restrict crack propagation reinforced the mortar's structural integrity. In conclusion, incorporating SF and hybrid fibers effectively improves mortar durability against HCl attacks. The findings highlight that the pozzolanic reaction of SF improves the durability of cement-based materials by enhancing the formation of C-S-H, which increases strength and reduces permeability. Additionally, the synergistic effect of hybrid fibers boosts crack resistance by distributing stress evenly and preventing crack propagation, offering valuable insights for optimizing cement mortar formulations in aggressive environments.

ARTICLE HISTORY
Received 21 December 2024
Accepted 26 January 2025

KEYWORDS
Cement mortar; silica fume; straight steel fiber; double hooked steel fiber; hydrochloric acid

1. Introduction

Acidic attacks pose substantial threats to the robustness and longevity of concrete structures, especially concerning the profound impact of hydrochloric (HCL) acid on an array of industrial and infrastructural elements. Exposure to HCL is ubiquitous in environments such as chemical plants, metal processing facilities, and transport infrastructure, exerting its influence on crucial elements, including concrete floor coatings, storage tanks, and drainage systems (Youssari et al., 2023; Madraszewski et al., 2023; Yoshida & Nakayama, 2023). The reactivity of HCL with fundamental constituents of concrete, notably calcium hydroxide (CH) and C-S-H bonds precipitates a series of structural weaknesses. This interaction initiates a process of dissolution, degradation, and material loss within the concrete matrix, compromising its inherent strength and durability (Ran et al., 2023; Zou et al., 2023; Muthu et al., 2021). Initiatives aimed at fortifying concrete structures against such corrosive assaults encompass the incorporation of pozzolanic substances, wherein silica fume (SF) emerges as a prominent candidate (Albattat et al., 2020; Taheri et al., 2020). SF, a residual product derived from the high-temperature production of silica dioxide, functions as an augmentative filler within the concrete matrix (Mehta & Ashish, 2020). Its intrinsic role involves compacting the internal structure of concrete and exhibiting notable pozzolanic activity (Nedunuri et al.,

CONTACT Zehra Funda Akbulut fundaakbulut@yyu.edu.tr Department of Mining Engineering, Faculty of Engineering, University of Van Yüzüncü Yıl, Van, Turkey.

© 2025 Informa UK Limited, trading as Taylor & Francis Group

2020; Wang et al., 2021). This unique characteristic fortifies the concrete's resistance against aggressive agents, such as HCL acids.

In contrast, the integration of steel (ST) fibers with diverse geometric configurations, mainly melt-extracted straight stainless steel (SST) and double-hooked steel (DHST) fibers, demonstrates promise in curtailing crack initiation and bolstering the structural integrity of concrete (Jiao et al., 2022; Abbass & Khan, 2022). SST fibers are produced using a rotating wheel by ejecting molten metal into the open air. SST fibers exhibit irregular and partially random geometry, owing to the manufacturing process allowing for a specific variability in fiber shape. These fibers are well-suited for use in environments prone to corrosion due to their stainless-steel composition (Huang et al., 2024). Additionally, they are commonly employed in refractory concrete, as they can withstand high temperatures (Zhang et al., 2021). However, due to their hooked ends, DHST fibers exhibit superior adhesion with concrete matrices compared to SST fibers. This enhanced adhesion arises from the mechanical interlocking provided by the hooked ends of DHST fibers within the concrete matrix. This feature enables DHST fibers to effectively distribute loads and resist crack propagation, enhancing concrete's overall performance and durability. Consequently, DHST fibers are often preferred in applications where robust bonding between the fiber and the concrete matrix is crucial, such as in high-performance concrete for infrastructure projects or industrial flooring systems subjected to heavy loads and dynamic stresses (Bao et al., 2024). Additionally, this robust interlocking facilitates effective stress transmission, thereby enhancing the mechanical properties of concrete, particularly in the aftermath of HCL exposure (Dezhampanah et al., 2020).

While DHST fibers offer distinct advantages over conventional reinforcements regarding cost efficiency, ease of implementation, and flexibility in reinforced concrete design, they present inherent challenges. These include susceptibility to potential corrosion, aesthetic considerations, workability issues during placement, the imperative of uniform distribution, and the associated costs (Lv et al., 2021; Raju et al., 2020). Consequently, a meticulous evaluation of their application and performance becomes imperative, aligning with specific project requirements and structural imperatives.

Enhancing the resilience and durability of concrete structures against acid attacks is paramount in construction materials. Utilizing pozzolanic materials in traditional concrete is vital in fortifying its ability to withstand acid aggression. These materials bolster the concrete's internal structure, thereby increasing its resistance to acid attacks. Pozzolanic substances react with cement during the hydration process, forming hydration products that densify the concrete matrix. Simultaneously, they react with acids to form compounds resistant to these agents, improving the concrete's strength and durability (Ahmad et al., 2022; Das et al., 2020). Specifically, materials like silica fume (SF) among the pozzolanic elements offer a practical approach to enhancing concrete's resilience against acidic attacks. SF, composed of microscopic particles, acts as a filler within the concrete matrix. Its filling effect densifies the structure, hindering acid penetration by occupying voids (Chaudhary & Sinha, 2020; Bilal et al., 2021).

Additionally, SF's high reactivity accelerates the formation of acid-resistant compounds, augmenting concrete durability (Ahmad et al., 2022). Besides, substituting Portland cement (PC) with SF signifies a significant stride toward sustainability in construction materials. Reducing carbon dioxide (CO_2) emissions associated with cement production minimizes environmental impact (Campos et al., 2020). Furthermore, SST and DHST fibers are crucial in limiting the occurrence and spread of micro and macro cracks within concrete because of HCL attacks. These cracks weaken concrete's load-bearing capacity, allowing environmental factors like acidic substances to penetrate. By incorporating SST and DHST fibers, these cracks are effectively deterred, enhancing the overall uniformity of concrete and restraining crack development (Paul et al., 2020; Ghaffary & Moustafa, 2020; Zia et al., 2023).

Moreover, these fibers also hinder the expansion of larger cracks, preserving the material's structural integrity. This situation contributes to bolstering concrete's durability against various external factors, ultimately extending the lifespan of structures and significantly reducing maintenance and repair expenses (El-Wafa, 2023; Ramasamy et al., 2020).

This study explores the workability, residual strength, and durability of mortars incorporating SF, SST, and DHST fibers under HCL exposure. It compares the effects of SST and DHST fibers on concrete's performance, specifically its resistance to acid attacks and its ability to maintain structural integrity. The research evaluates how these fibers influence fresh mortar properties, including flow diameter (FD), as well as changes in apparent porosity (AP), water absorption (WA), and strength after HCL exposure. The study also investigates the residual compressive and flexural strength of mortar samples. Finally, SEM analysis was used to examine the impact of HCL on the internal composition of the mortar.

2. Material and method

2.1. Materials used in the mortar mixes

CEM I 42.5 R Portland cement (PC) and silica fume (SF) were utilized as binding materials in the mortar blends. The SF used exhibited a BET-specific surface area (SSA) measured at 150 m^2/g and was incorporated into the mortar mixtures by replacing 10% of the cement by weight. The fine aggregate material in these blends consisted of CEN standard sand, boasting a silicon dioxide content of at least 98%. A polycarboxylate-based superplasticizer (SP) supplement was employed throughout the experiments to ensure consistent water levels and achieve the desired workability. Mains water was used exclusively during the experiments, free from contaminants or substances that might compromise the cement's durability. The study used micro-melt extracted straight stainless steel (SST) fibers, 20 mm long, and double-hooked steel (DHST), 35 mm long, as steel fibers. Similar aspect ratios (length/diameter) were selected for a more meaningful comparison between SST and DHST fibers. The aspect ratio for SST fibers was 50, while for DHST fibers, it was 45. The tensile strength of micro-SST fibers is 540 MPa, whereas, for macro-DHST fibers, it is 1100 MPa. Figure 1 provides visual references depicting the appearances of silica fume (SF), micro-SST, and macro-DHST fibers utilized in this study. Detailed technical characteristics of the Portland cement (PC) and silica fume (SF) utilized are presented in Table 1. The technical properties of micro-SST and macro-DHST fibers are given in Table 2. X-ray diffraction (XRD) and scanning Electron Microscope (SEM) analysis of PC and SF materials were meticulously displayed in Figures 2 and 3, respectively.

2.2. Preparation of mortar mixes and production of examples

The study formulated eight blends, one serving as a control mix (TS EN 196-1,1, 2009). The composition of P0–P7 blends is outlined in Table 3. Notably, the P0 blend is a control mix, and the P1 blend exclusively featured silica fume (SF), P2–P3 blends integrated 20 mm micro-SST fibers with SF, P4–P5 blends incorporated 35 mm macro-DHST fibers alongside SF, P6–P7 blends combined 20 mm micro-SST and 35 mm macro-DHST fibers in conjunction with silica fume (SF). The overall volumetric ratios of macro-ST and micro-PP fibers in these blends were maintained at 0.5% and 1%, respectively. The blend codes represented the percentages of SF, SST, and DHST fibers. For instance, "SF10_DHST35_0.8_SST20_0.2%" indicated a blend with a 0.8% volumetric ratio of 35 mm DHST fibers and 0.2% 20 mm SST fibers combined with 10% SF. A consistent water/cement ratio of 0.5 was upheld across all combinations to compare the influence of micro-SST and macro-DHST fibers on flow diameters (FD) within the blends. Adding a superplasticizer (SP) was crucial to ensure optimal FD in blends containing micro-SST and macro-DHST fibers, preventing accumulation and facilitating mold placement. Determining the optimal SP ratio involved iterative trial and error methods. SP was absent in the P0 control blend. For the P1 blend using only SF, the SP ratio was 0.1% of PC. Blends with a 0.5% total fiber ratio employed an SP ratio of 0.5% of PC, while blends with a 1% total fiber ratio used an SP ratio of 1% of PC. In preparing the mixtures labeled P0–P7, the process begins by mixing 50% of PC, SF, and standard sand and 50% of the total mixing water for 2 min. Then, the remaining 50% of the water, mixed beforehand with SP, is added to the blend and mixed for another 2 min. After this, micro-SST and macro-DHST fibers are manually introduced into the mixtures and blended for 2 min. The process continued after blending the fresh mixtures. Initially, the



(a) SF (b) Micro-SST (c) Macro-DHST

Figure 1. The view of SF, SST, and DHST fibers.

Table 1. Chemical, physical, and mechanical properties of Portland cement and silica fume (SF).

Chemical properties	SiO_2	21.56%
	Al_2O_3	5.97%
	Fe_2O_3	2.88%
	CaO	60.51%
	MgO	2.94%
	SO_3	2.91%
	Na_2O	–
	K_2O	0.76%
	Cl	0.01%
Physical properties	Initial setting time	157 mins
	Final setting time	223 mins
	Specific gravity	3.18 g/cm^3
	Specific surface	3984 cm^2/gr
Compressive strength (MPa)	After 2 days	22.7
	After 7 days	41.6
	After 28 days	51.9

Table 2. Technical properties of SST and DHST fibers.

	Length (mm)	Diameter (mm)	Aspect ratio (L/D)	Spesific Gravity	Tensile strength (MPa)	Elastic modulus (GPa)
SST	20	0.47	50	7.85	540	125
DHST	35	0.75	45	7.85	1100	205

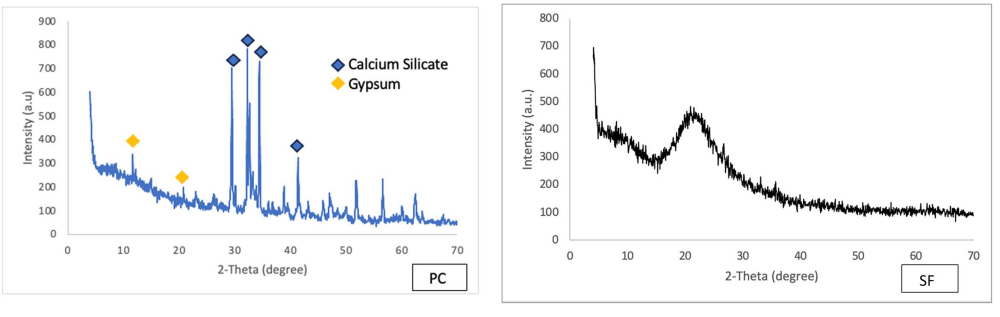

Figure 2. The XRD patterns of PC and SF materials at ambient conditions.

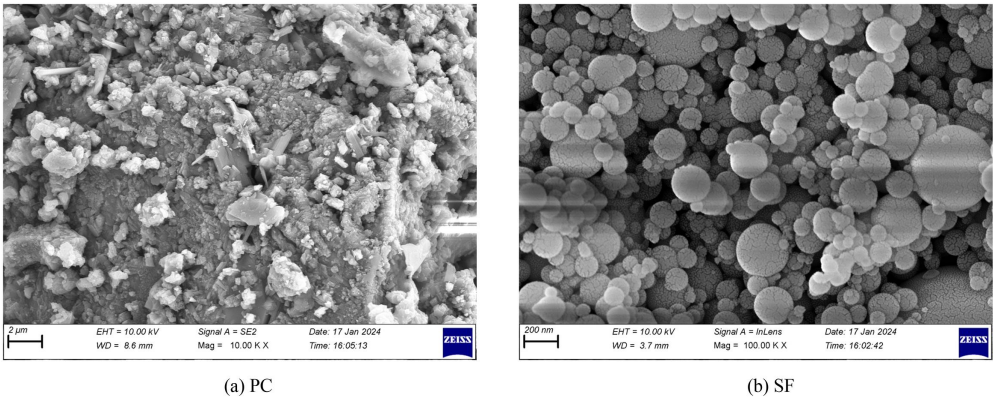

(a) PC (b) SF

Figure 3. The SEM images of PC and SF materials at ambient conditions.

FD rates were measured using the mini-spreading table. The freshly prepared mortars were poured into cubes measuring $50 \times 50 \times 50\,mm^3$ and prismatic molds measuring 40×40 x $160\,mm^3$. Once filled, the molds containing the fresh blends were settled onto a shaking table and vibrated for approximately 2 min. After a resting period of 24 h, all specimens were removed from the molds and placed in a

Table 3. Mix-design of the P0–P7 mixes.

Mixes	Mix Code	Cement (g)	SF (g)	Sand (g)	Water/ Cement	SP (%)	20 mm SST fiber (%)	35 mm DHST fiber (%)
Control	P0	450	–	1350	0.5	–	–	–
SF10	P1	405	45	1350	0.5	0.1	–	–
SF10_SST20_0.5%	P2	405	45	1350	0.5	0.5	0.5	–
SF10_SST20_1%	P3	405	45	1350	0.5	1	1.0	–
SF10_DHST35_0.5%	P4	405	45	1350	0.5	0.5	–	0.5
SF10_DHST35_1%	P5	405	45	1350	0.5	1	–	1.0
SF10_DHST35_0.35_SST20_0.15%	P6	405	45	1350	0.5	0.1	0.15	0.35
SF10_DHST35_0.8_SST20_0.2%	P7	405	45	1350	0.5	0.5	0.2	0.8

standard curing pool with water for 28 days. Subsequently, these specimens were transferred into plastic buckets containing a 5% hydrochloric acid (HCL) solution for 7, 28, and 56 days for further testing and evaluation.

2.3. Testing procedure applied in the study

The blends' flow diameter (FD) values were assessed in two perpendicular directions using a mini-spreading table, and their mean values were documented (ASTM C1437,1437, 2015). Post the 28-day curing period, specimens were retrieved from the curing pool and subjected to desiccation at 105 °C in an oven. Subsequently, the specimens' mass, visible porosity, ultrasonic pulse velocity (UPV), compressive strength, and flexural strength were determined. Following this initial evaluation, all specimens underwent immersion in 5% HCL solutions contained in plastic receptacles. Evaluations were conducted on days 7, 28, and 56 to ascertain the specimens' WA (ASTM International & ASTM C1585-13,13, 2013), AP (American Society for Testing & Materials ASTM C642,642, 2013), ML, RDME (ASTM C 597, 597, 2016), RCS (ASTM C109,109, 2013), and RFS (ASTM C348,348, 2014) values. The specimens' resistance to HCL attacks was appraised per ASTM C267 standard (ASTM C267,267, 1997). Renewal of the HCL solutions occurred weekly, maintaining a consistent pH level of 1.5 ± 0.05 throughout the 7, 28, and 56-day periods. The pH levels in the HCL solutions were vigilantly monitored using a portable digital pH meter to ensure uniformity. Evaluations concerning WA, AP, ML, RDME, and RFS values, both under standard conditions and after exposure to HCL attacks, were conducted using prismatic specimens sized at $40 \times 40 \times 160\ mm^3$. The RCS rates of the specimens were determined utilizing cube-shaped specimens, each measuring 50 mm. The samples' WA, AP, ML, RDME, RCS, and RFS values were determined following the applicable standards. Three samples from each blend were tested for each parameter, and the resulting averages were computed. The calculations for the samples' WA, AP, ML, RDME, RCS, and RFS values were derived using the relationships outlined in Equations (1)–(5).

$$AP = \frac{W_{sd} - W_k}{W_{sd} - W_w} \tag{1}$$

$$WA = \frac{W_{sd} - W_k}{W_k} \tag{2}$$

$$RCS = \frac{R_{ci} - R_{co}}{R_{co}} x100 \tag{4}$$

$$RFS = \frac{F_{ci} - F_{co}}{F_{co}}\ x\ 100 \tag{5}$$

$$\mathrm{ML}(\%) = \frac{W_{ni} - W_{oi}}{W_{oi}}\ \mathrm{x}\ 100 \tag{6}$$

$$\mathrm{RDME}(\%) = \frac{UPV_n^2}{UPV_o^2}\ \mathrm{x}\ 100 \tag{7}$$

In this context, Wsd represents sample weight in a saturated yet surface-dry state. Wk denotes the weight of samples when thoroughly dried in an oven. Ww refers to sample weight under saturation when immersed in water. Rco and Rci signify the comparative compressive strength ratios before and after exposure to HCL attacks. Fco and Fci indicate the comparative ratios of flexural strength before and

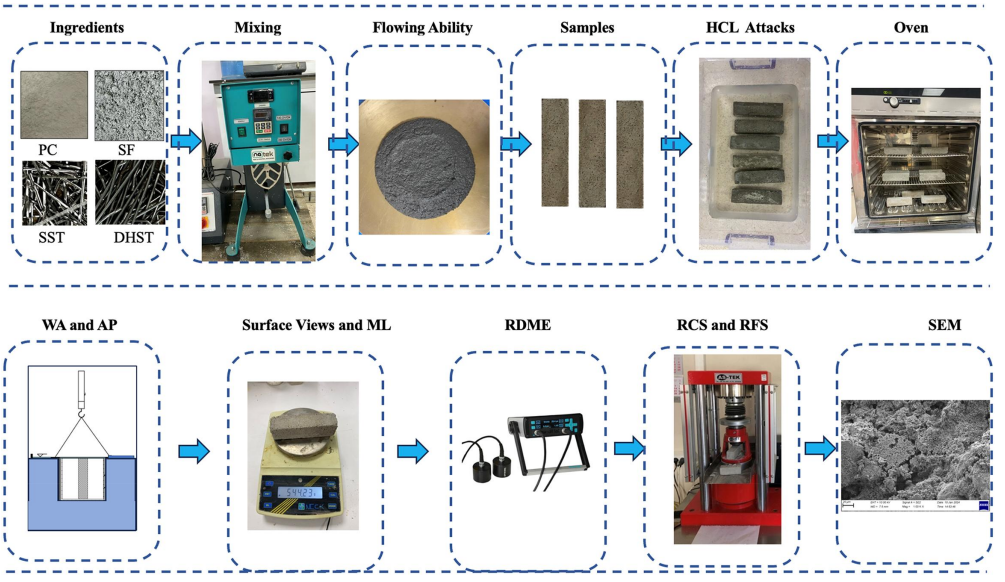

Figure 4. The schematic view of the preparing and testing stages of P0–P7 mixes.

after exposure to HCL attacks. Woi and Wni represent sample weight pre- and post-HCL attacks. UPVo and UPVn gauge the speed of ultrasonic pulses through mortar samples in standard ambient conditions and post-HCL attacks.

The cured mortar samples underwent initial grinding using a mortar grinding device to perform XRD analysis. The XRD analysis was conducted utilizing CuKα radiation, which was generated by applying 40 kV voltage and 15 mA current to the Cu tube through the Rigaku Mini Flex 600 device. Assessments were conducted within a temperature range of 17 to 70 °C, with a 1°/min gain and a scanning speed of 0.02°. For the evaluation of changes in the internal structures post-HCL attacks, SEM analysis was performed on P0, P1, and P7 specimens. SEM analyses were conducted under standard ambient conditions and after exposure to HCL attacks for 7, 28, and 56 days. Each specimen's SEM images were captured at 1×1000 magnifications. Figure 4 provides a schematic depiction outlining the sequential procedures involving the specimens' preparation, molding, and subsequent testing.

3. Results and discussion

3.1. Flow diameter (FD) rates of the P0–P7 blends

Fresh mortar flow diameter (FD) values are key indicators of workability, with higher FD values reflecting better workability. Figure 5 shows the results of the mini-spreading test, and Figure 6 presents FD values after the spreading test for all samples. The control sample (P0) had an FD of 192 mm, while P1 with 10% SF had 174 mm, and P2–P3 with micro-SST fibers had FD values of 161 mm and 143 mm, respectively. Furthermore, the P4–P5 examples featuring macro-DHST fibers displayed FD values of 152 mm and 128 mm, while the P6–P7 examples utilizing hybrid SST/DHST fibers demonstrated FD values of 156 mm and 134 mm. These results, as showcased in Figure 6, indicate the SP usage across various blends: absent in the P0 control, at 0.1% for blends with 10% SF additives, 0.5% for blends with 0.5% SST and DHST fiber content, and 1% for blends with 1% SST and DHST fiber content. Notably, it's discerned that employing a superplasticizer (SP) is crucial to achieving adequate flowability, particularly in blends involving SF, micro-SST, and macro-DHST fibers when measuring the FD value of fresh mortars. Fiber clumping occurs when the SP ratio falls below the optimum level, hampering accurate FD measurements in the blends. Conversely, excessive SP usage leads to water segregation and component separation within the blends (Lai et al., 2022; Sposito et al., 2022). Introducing silica fume (SF) materials increases the water



Figure 5. The views of flow diameter (FD) of P0, P1, and P7 fresh mixtures on the spreading table.

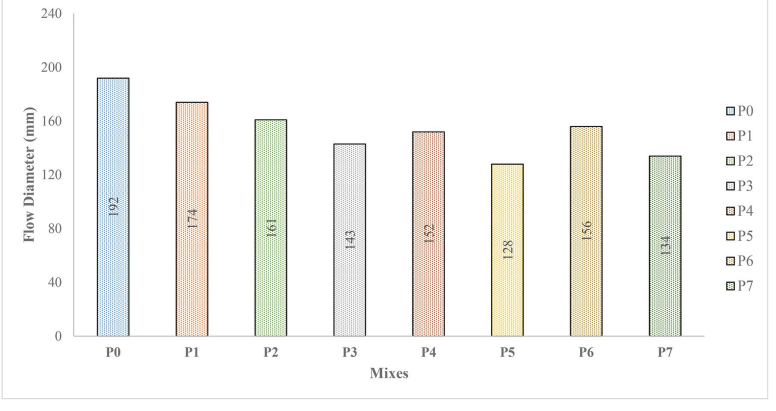

Figure 6. The values of flow diameter (FD) of P0–P7 mixtures.

demand within the blends (Ma et al., 2022), primarily due to the high-water absorption of SF agglomerates owing to their substantial specific surface areas.

Moreover, adding SF augments friction forces within the blends, heightening plastic viscosity and diminishing blend fluidity (Liu et al., 2021). Adding micro-SST and macro-DHST fibers to the mixes has negatively affected the flowability of the blends and caused FD values to be significantly decreased. In the blends where micro-SST macro-DHST fibers are used, it was seen that micro-SST and macro-DHST fibers tend to clump and cluster in a region of the blend and do not exhibit a homogeneous distribution (Carrillo et al., 2021). However, it's observed that the workability of mortar with macro-DHST fiber additives is more adversely affected than that of micro-SST fibers, resulting in lower FD values. The hooked ends of macro-DHST fibers increase friction between the fibers, causing them to entangle and consequently reducing the flowability and FD values of the mixtures.

Additionally, the higher adhesive strength of the hooked ends of macro-DHST fibers to the matrix compared to micro-SST fibers is another reason for the mixtures' decreased flowability and FD values. Additionally, with the increase in fiber ratio from 0.5% to 1%, the intensified inter-fiber friction notably exacerbated the reduced flowability in the blends, leading to a more pronounced decline in FD values. Consequently, to mitigate fiber agglomeration and ensure a more uniform dispersion, the contribution rate of the SP was elevated from 0.5% to 1% upon the escalation of the fiber ratio from 0.5% to 1%. In contrast to the exclusive use of macro-DHST fibers in P4–P5 blends, incorporating micro-SST and macro-DHST fibers in hybrid form in P6–P7 blends resulted in marginally improved flowability and, consequently, slightly higher FD values. The main reason for this improvement is that the 35 mm-long macro-DHST fibers were replaced by 20 mm-long micro-SST fibers in the mixtures. This replacement reduced the friction between the fibers, allowing them to move more freely, which in turn improved the overall flowability of the blends.

3.2. water absorption (WA) and apparent porosity (AP) of the P0–P7 blends

Acidic infiltration into the inner framework of solidified concrete triggers a process of expansion and degradation recognized as an acid attack, significantly undermining the structural integrity. Among the potent acids, HCL stands out for its pronounced corrosive impact, notably compromising the strength and durability of conventional concretes reliant on PC binders (Pather et al., 2021). To bolster the resilience of these concrete structures against HCL assaults, reinforcing their interior with synthetic pozzolanic substances like SF becomes imperative. Crucial parameters such as WA and AP serve as fundamental indicators, reflecting the permeability characteristics of these concrete specimens. Elevated WA and AP values are indicative of escalated permeability. Figures 7 and 8 portray the WA and AP values for specimens labeled P0–P7, illustrating the rise in WA and AP rates following exposure to HCL for 7, 28, and 56 days compared to baseline conditions. For example, after 7 days of exposure to HCL acid attacks, compared to ambient conditions, the WA rates increased by 27.73% for P0, while P1, with SF, showed a rise of 26.62%. Similarly, P2–P3, incorporating micro-SST fibers, exhibited increases ranging from 26.52% to 24.75% in WA rates. Macro-DHST fiber-based P4–P5 experienced a surge of 26.26% and 23.75% in WA rates, while hybrid SST/DHST fiber-utilizing P6–P7 showcased increases ranging from 25.96% to 23.46%. After 56 days, P0 exhibited a surge of 145.86% in AP rates, P1 showed a rise of 128.73%, and P2–P3 demonstrated increases ranging from 117.97% to 113.30%. Furthermore, P4–P5 experienced a surge of 112.95% and 110.28% in WA rates, while P6–P7 exhibited elevations between 112.48% and 109.83%. Additionally, the data presented in Figure 8 illustrates the increase in AP rates following exposure to HCL compared to ambient conditions. After 7 days of exposure, P0 showed a 40.65% increase in AP, P1 with SF displayed a 33.77% increase, and P2–P3 with micro-SST fibers ranged between 34.53% and 36.26%. Similarly, P4–P5 incorporating macro-DHST fibers manifested a 36.12% and 38.48% increase in AP, while P6–P7 utilizing a

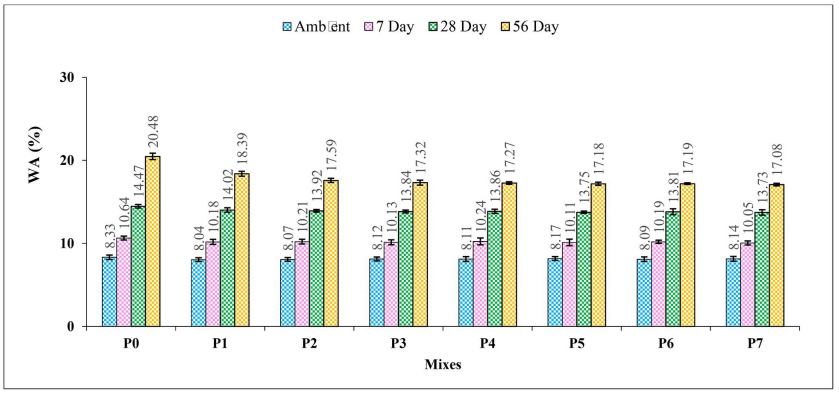

Figure 7. The values of water absorption (WA) of P0–P7 mixtures.

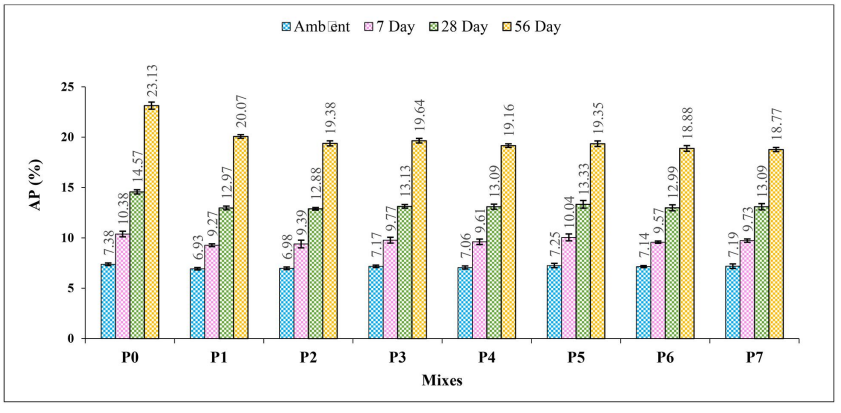

Figure 8. The values of apparent porosity (AP) of P0–P7 mixtures.

hybrid SST/DHST fiber combination showcased AP increments ranging from 34.03% to 35.33%. Following 56 days, P0 experienced a significant 213.41% surge in AP, P1 displayed a 189.61% rise, P2–P3 samples revealed increases ranging between 177.65% and 173.92%, P4–P5 showcased a 171.39% and 166.90% AP increase, and P6–P7 exhibited increments between 164.43% and 161.06%. These findings underscore the consistent elevation in absorption rates across varied concrete compositions under HCL exposure, emphasizing the criticality of fortifying concrete structures against acid-induced decay to ensure sustained resilience. The utilization of SF effectively mitigates WA and AP rates by addressing internal structural voids. While micro-SST and macro-DHST fibers contribute to reducing WA and AP values in some cases, their hybrid application demonstrates lower increments in WA and AP compared to singular micro-SST usage. The negative influences of micro-SST and macro-ST fibers in increasing WA and AP might be attributed to the voids they create in the structure (Ali et al., 2020). Hybrid SST/DHST fibers efficiently bridge cracks induced by HCL attacks, creating a more impermeable internal network (Zhang et al., 2023). Additionally, substituting macro-DHST fibers with micro-SST in hybrid blends minimizes internal cavities, sealing micro-gaps and cracks more effectively.

3.3. Mass loss

The visual assessment and measured ML values of the specimen's post-exposure to HCL attacks for 7, 28, and 56 days are displayed in Figures 9 and 10, respectively. The transition from smoother surfaces pre-HCL exposure to rougher, porous textures post-attack is evident in Figure 9, indicating surface alteration due to HCL. Notably, the increased shedding observed in specimens exposed for 56 days highlights a direct correlation between prolonged exposure and higher ML. Correspondingly, Figure 10 demonstrates ML escalation under prolonged HCL exposure. For instance, after 7 days, P0 showed a 4.09% increase ML, while P1 (SF-based) exhibited a 3.96% rise. Similarly, micro-SST-incorporated P2–P3 showcased ML increases ranging between 3.84% and 3.87%. Macro-DHST-infused P4–P5 experienced a surge of 3.88% and 3.85% in ML, while hybrid SST/DHST-employed P6–P7 displayed increases ranging from 3.90% to 3.93%. After 56 days, P0 demonstrated an 11.38% surge in ML, P1 exhibited an 11.07% rise, and P2–P3 displayed increases ranging between 11.04% and 11.09%. Furthermore, P4–P5 experienced a 10.94% and 11.03% increase in ML, while P6–P7 exhibited elevations between 10.91% and 11.01%. Examining Figure 10 reveals a clear link between the ML values and the duration of exposure to HCL. Specimen P1, with SF as the sole addition, shows slightly lower ML values than the control sample P0. SF contributes by bolstering the interior's resistance to HCL penetration, thereby minimizing harmful ion intrusion (Paruthi et al., 2023). However, its limitation in averting surface peeling impacts its effectiveness on ML rates (Fattouh et al., 2023). Additionally, the combinations of micro-SST, macro-DHST fibers, and SF exhibit reduced ML rates compared to the P0 control specimen. Yet, specific samples with micro-SST and

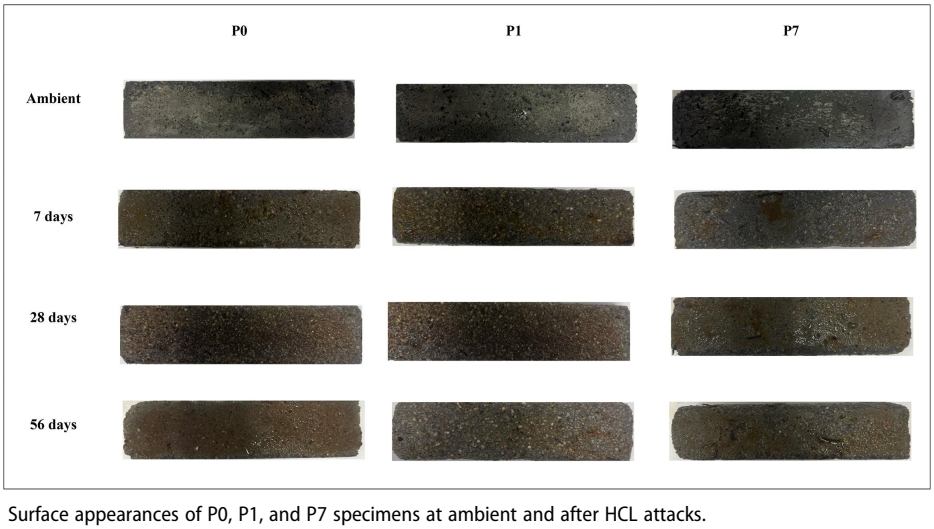

Figure 9. Surface appearances of P0, P1, and P7 specimens at ambient and after HCL attacks.

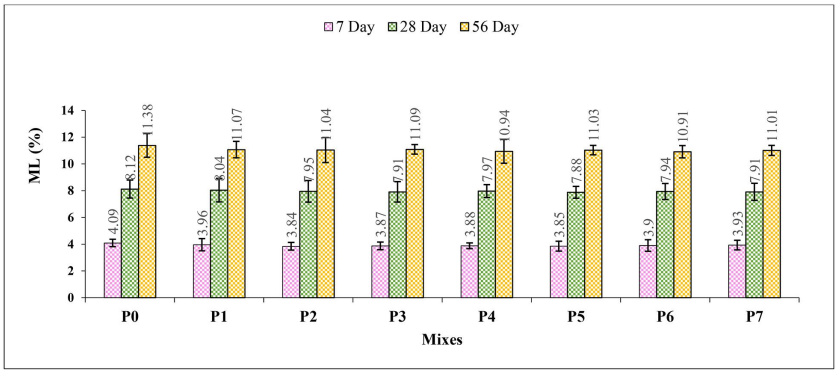

Figure 10. The mass loss (ML) values of P0–P7 specimens after HCL attacks.

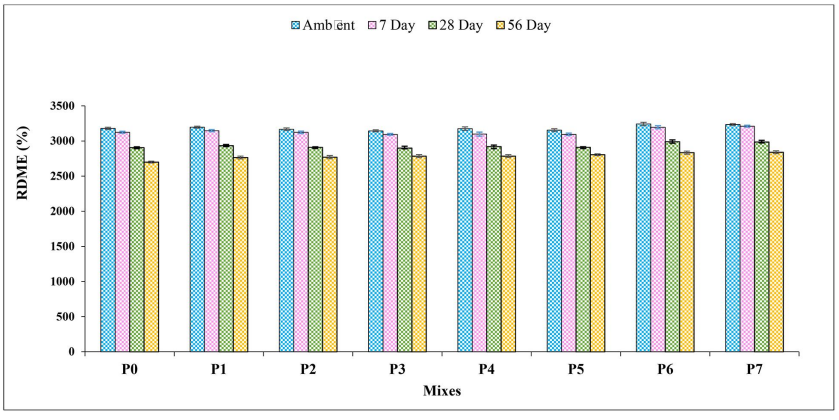

Figure 11. The relative dynamic modulus of elasticity (RDME) values of P0–P7 specimens after HCL attacks.

macro-DHST fibers showcase ML rates nearly equal to or slightly surpassing the SF-assisted P1 specimen. This inability is attributed to the collective incapacity of these fibers and SF to prevent surface shedding post-exposure to HCL (Chen et al., 2023). Furthermore, the comparative advantage of using a hybrid approach with micro-SST and macro-DHST fibers in ML reduction remains inconclusive when contrasted with their singular applications.

3.4. RDME of P0–P7 blends

Figure 11 illustrates the decline in RDME rates across examples P0–P7 following exposure to HCL attacks. RDME values serve as indicators reflecting the level of damage inflicted on the internal network structures of these samples. Higher RDME values signify a more intact and less damaged internal structure, as ultrasonic waves propagate faster through undamaged structures. HCL attacks induced cavities within the examples' interior networks, forming voids and cracks of varying sizes (Shariati et al., 2021). A consistent decrease in RDME values was observed across all examples subjected to 7, 28, and 56 days of HCL exposure, directly proportional to the duration of exposure. More extended exposure periods led to more pronounced damage within the internal structures. Examining Figure 11, After 7 days, P0 showed a 1.76% decrease in RDME, while P1 (SF-based) displayed a 1.56% decrease. Similarly, examples P2–P3, which integrated micro-SST, exhibited RDME reductions ranging between 1.36% and 1.62%. P4–P5 with macro-DHST experienced a decrease of 2.42% and 1.90% in RDME, and P6–P7, employing hybrid SST/DHST, showed decreases spanning from 1.45% to 0.74%. Over 56 days, P0 demonstrated a 15.09% decrease in RDME, P1 exhibited a 13.51% decrease, and P2–P3 displayed reductions ranging between 12.54% and

11.45%. Additionally, P4–P5 encountered a 12.31% and 11.09% decrease in RDME, whereas P6–P7 exhibited variations between 12.58% and 12.21%. SF, ST, and PP fibers showcased slight effectiveness in mitigating RDME value decreases post-HCL attacks, resulting in marginally lower RDME values in examples P1–P7 compared to the P0 control. SF usage demonstrated a modest impact in averting RDME value reduction by effectively filling post-HCL attack gaps within the internal network, acting as a filler (Bin, 2021). Furthermore, including micro-SST and macro-DHST fibers alongside SF effectively restrained RDME reduction in these examples. This positive contribution is attributed to their efficacy in limiting interior network cracks post-HCL attacks by bridging them (Zeng et al., 2020). Notably, hybrid blends containing both SST and DHST fibers exhibited slightly lower RDME reductions compared to those with only SST fibers. This difference can be attributed to the superior crack-sealing ability of micro-SST fibers, which are more efficient in filling and preventing the spread of micro-cracks after exposure to HCL attacks. In contrast, macro-DHST fibers are less effective in sealing these small cracks, leading to greater damage and a higher reduction in RDME. As a result, the combination of SST and DHST fibers provides a better overall performance by leveraging the strengths of both fiber types in resisting chemical degradation (Shin & Yoo, 2020). It's crucial to note that the RDME values obtained for samples P0–P7 after HCL attacks are closely aligned. Thus, the impact of SF, SST, and DHST fibers in curbing RDME reductions may be more evident in examples subjected to prolonged HCL exposure. They expect their combined use to be more effective in enhancing RDME rates in examples enduring more prolonged HCL attacks, potentially surpassing the control example's RDME values as these longer exposures cause more significant interior structure damage.

3.5. Residual compressive strength

Figure 12 illustrates the residual compressive strength (RCS) rates of examples P0–P7 following 7, 28, and 56 days of HCL attacks. Initially, after 7 days, P0 exhibited a 12.85% decrease in RCS, while P1 (SF-based) showed a reduction of 10.24%. Similarly, P2–P3, incorporating micro-SST, demonstrated RCS reductions ranging from 8.98% to 7.29%. P4–P5, with macro-DHST, experienced decreases of 7.93% and 6.60% in RCS, while P6–P7, utilizing hybrid SST/DHST fibers, exhibited reductions ranging from 6.87% to 6.35%. Over 56 days, P0 showcased a 40.73% decrease in RCS, P1 exhibited a 37.11% reduction, and P2–P3 displayed decreases ranging between 34.71% and 32.31%. Furthermore, P4–P5 encountered decreases of 31.88% and 28.86% in RCS, whereas P6–P7 showed variations ranging between 30.96% and 28.13%. These findings indicate substantial reductions in the RCS capacities of P0–P7 examples post-HCL attacks. Notably, these reductions were more pronounced in examples exposed to HCL for 28 and 56 days compared to 7 days, signifying a time-dependent exacerbation. Moreover, the singular and combined utilization of silica fume (SF), micro-SST, and macro-DHST fibers manifested a significant synergy in enhancing the RCS capacities of specimens against HCL attacks. Examining the SF-based P1 sample revealed lower RCS rate reductions post-HCL attacks compared to the P0 control example. This effect is attributed to SF's ability to effectively fill interior structure gaps, displaying a micro-filling effect (Song et al., 2020).

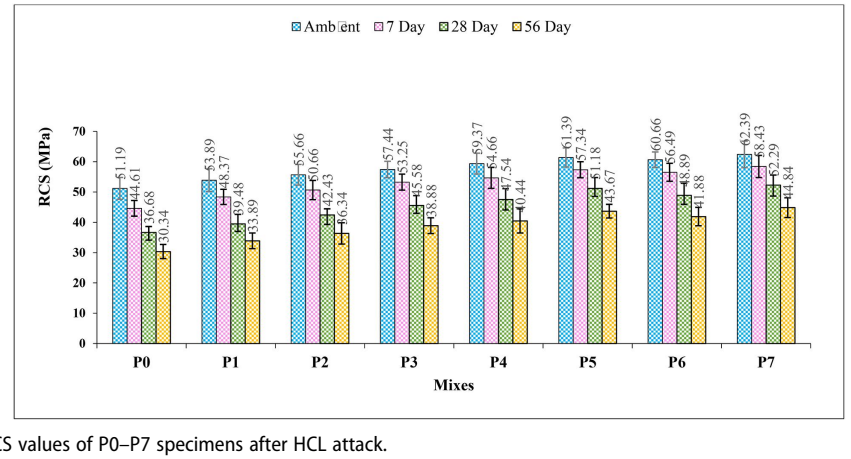

Figure 12. RCS values of P0–P7 specimens after HCL attack.

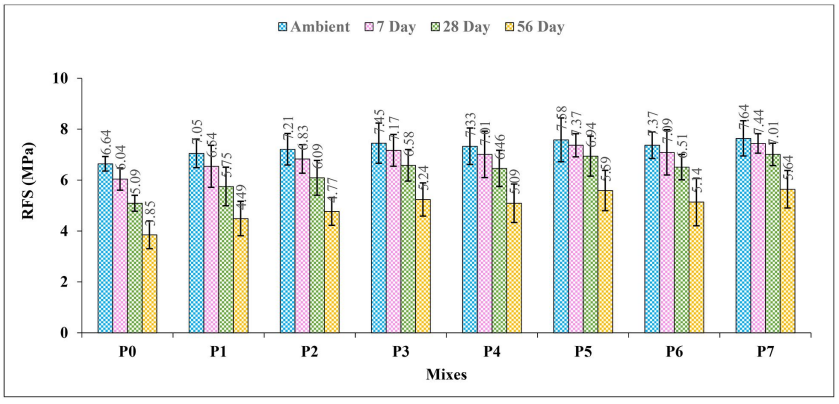

Figure 13. RFS values of P0–P7 specimens after HCL attacks.

Additionally, SF induces the formation of new C-S-H bonds within the network due to pozzolanic reactions with hydration products like portlandite (CH) (Li et al., 2023). Furthermore, incorporating micro-SST and macro-DHST fibers in blends enhanced compressive strength post-HCL attacks, resulting in mitigated RCS reductions. The strong adherence effect between these fibers and the sample matrices significantly preserved example integrity (Wang et al., 2020). Macro-DHST fibers particularly limited and bridged macro-cracks within the internal network post-HCL attacks, preventing their rapid and uncontrolled spread (Huang et al., 2023).

3.6. residual flexural strength

Figure 13 showcases the residual flexural strength (RFS) rates of P0–P7 specimens following exposure to HCL attacks for 7, 28, and 56 days. After 7 days, P0 showed a decrease in RFS by 9.04%, while P1 (SF-based) had a reduction of 7.23%. Similarly, samples incorporating micro-SST (P2–P3) exhibited RFS reductions between 5.27% and 3.76%. P4–P5, integrating macro-DHST, experienced a considerable decrease of 4.37% and 2.76%, whereas P6–P7, utilizing hybrid SST/DHST fibers, showed variations between 3.80% and 2.62%. At the 56-day HCL attacks, P0 demonstrated a profound 42.02% reduction in RFS, P1 showcased a 36.31% decrease, and P2–P3 maintained reductions between 33.84% and 29.66%. Furthermore, P4–P5 encountered a moderate decrease of 30.56% and 26.25% in RFS, while P6–P7 exhibited variations from 30.26% to 26.18%. These findings underscore the compelling impact of SF, micro-SST, and macro-DHST fibers in fortifying the RFS capacities post-HCL attacks. SF's ability to fill voids within the matrix and create additional C-S-H bonds resulted in tighter structures and heightened RFS capabilities (Akarsh et al., 2021). Additionally, combining micro-SST and macro-DHST fibers with SF effectively countered the decline in RFS capacities. Moreover, the hybrid use of micro-SST with macro-DHST fibers demonstrated a slightly lesser reduction in RFS than the singular application of macro-DHST fibers. The hooks on both ends of macro-DHST fibers establish robust adherence within the network, contributing to higher RFS capacities (Al-Osta et al., 2021). These fibers play crucial roles in bridging cracks, preventing their uncontrolled spread towards the neutral axis and delaying micro-cracks progression. Thus, this leads to a marginally increased RFS rate compared to using macro-DHST fibers singularly. Illustrating the enhancement of structural integrity against HCL attacks by improving internal network features through SF, micro-SST, and macro-DHST fibers, Figure 14 schematically demonstrates this paradigm shift.

3.7. Microstructure analyses of cement mortars

In hardened concrete, the infiltration of acidic substances due to external factors can lead to expansion, resulting in cracks and internal stresses that cause deterioration. This phenomenon, known as "acid attack," mainly targets the gel-like components encompassing hydrate, silica, calcium, and calcium hydroxide (CH) within fully cured concrete. The impact of these acids on concrete integrity is far-reaching, especially concerning the principal ingredients, cement and aggregate, rendering them highly

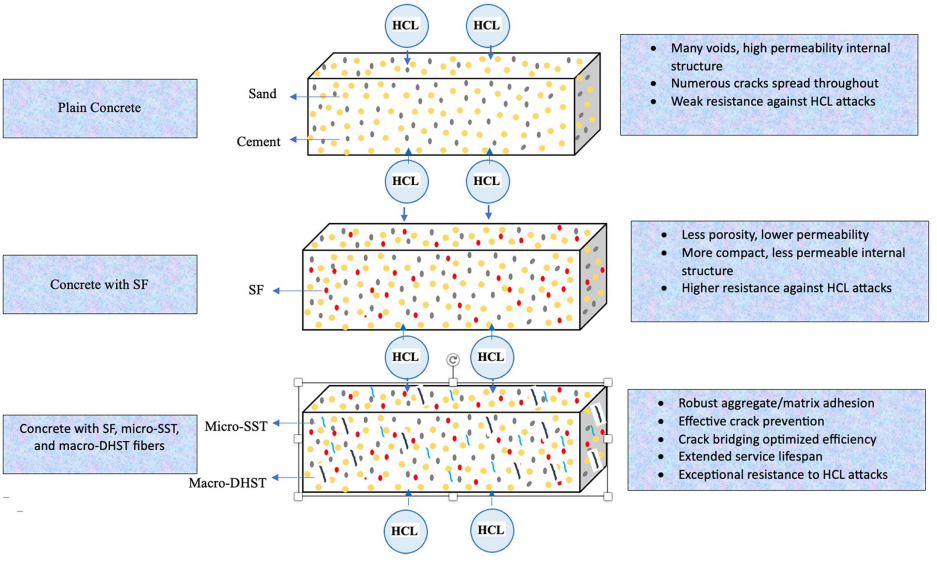

Figure 14. A schematic representation of the contribution of SF, micro-SST, and macro-DHST fibers to the internal structure of mortar samples in the face of HCL attacks.

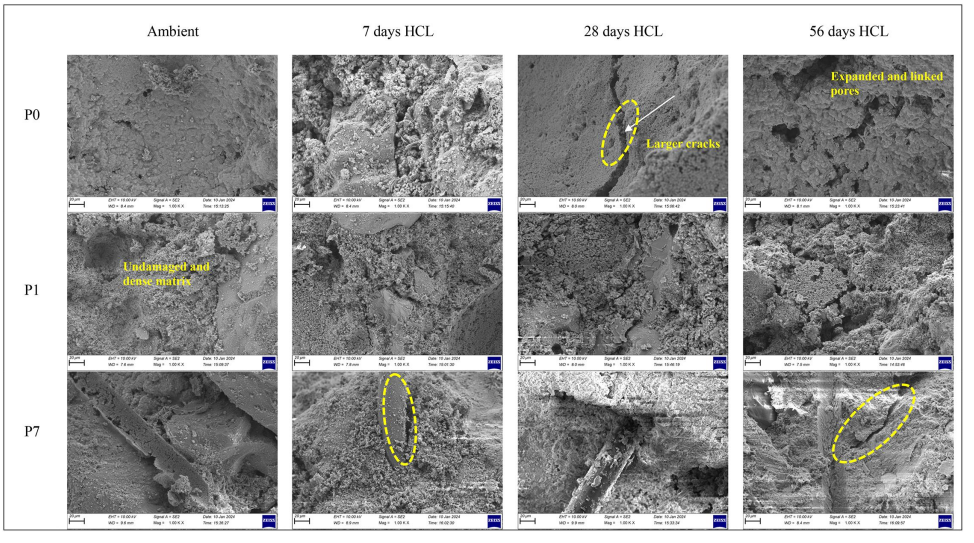

Figure 15. SEM images of P0, P1, and P7 specimens at ambient conditions after HCL attacks.

vulnerable to damage when combined with water (Paruthi et al., 2023). HCL acid is one of the most corrosive acids, capable of dissolving carbonate-based particles within the concrete matrix. Consequently, this degradation leads to a thin and less substantial layer within the concrete, diminishing its load-bearing capacity and shortening its overall service life (Janowska-Renkas et al., 2021). Figure 15 illustrates the internal structural views of P0, P1, and P7 samples under ambient conditions and subsequent exposure to HCL attacks for 7, 28, and 56 days. Remarkably, under ambient conditions, all examples exhibit a stable internal structure. However, the extent of damage in samples exposed to prolonged HCL exposure directly correlates with the duration of the attack. The control sample, P0, exhibit a loss of stability and a significantly impaired internal network following prolonged exposure to HCL. This includes the manifestation of macro voids, cracks, micro-cracks, and voids, particularly observable in the network of the P0 sample exposed to 56 days of HCL attack. Micro voids and cracks initially formed during 7 and 28-day

exposures intensify over 56 days, culminating in macroscopic gaps and cracks throughout the entire network.

Consequently, significant deterioration in the RCS and RFS capacities is noted in the P0 control example post-HCL exposure. In contrast, the SF-added P1 sample demonstrates a more robust and stable internal network under ambient conditions and post-HCL attacks. The improved structural integrity in the P1 sample can be attributed to the filler effect of SF, effectively filling micro and macro cavities, along with the additional formation of C-S-H bonds within the network (Frýbort et al., 2023). Moreover, the hybrid approach in the P7 sample, incorporating macro-DHST and micro-SST fibers in addition to SF, displays a more compact and less damaged internal structure than the P0 and P1 examples. The macro-DHST fibers act as bridges, inhibiting the propagation of macro cracks throughout the network, resulting in fewer and shallower cracks (Shi et al., 2023). Additionally, the micro-SST fibers effectively fill micro-gaps, impeding micro-cracks' evolution into macro-cracks. Consequently, both P1 and P7 samples exhibit reduced permeability and heightened RCS and RFS rates compared to the P0 control example, indicating enhanced resistance to HCL-induced deterioration.

4. Conclusions

The exploration delved into enhancing workability and traditional cement mortars' physical and mechanical traits before and after facing HCL assaults, employing SF, micro-SST, and macro-DHST fibers in singular and hybrid formats. The key findings from the investigation are detailed below:

- HCL exposure leads to notable degradation of both the internal composition and external surfaces of the specimens. Continued contact with HCL acid intensifies this damage, gradually compromising the material's structural integrity and surface properties.
- The optimum use of a superplasticizer (SP) is pivotal when integrating micro-SST and macro-DHST fibers, ensuring seamless dispersion without clumping in the blends.
- Because of a larger specific surface area, silica fume (SF) adversely impacts all the blends' flow diameter (FD) values. However, SF fortifies physical and mechanical features by effectively filling interior structure voids (filler effect) and instigating new C-S-H bonds within the network.
- The synergistic alliance between micro-SST and macro-DHST fibers with SF notably elevates the RCS and RFS rates post-HCL attacks.
- Micro-SST and macro-DHST fibers do not markedly diminish mass loss (ML) rates post-HCL attacks due to their insufficiency in preventing dissolution and peeling on the specimens' outer surfaces.
- The inclusion of DHST fibers with hooked ends has adversely affected the workability of the mixtures compared to mixtures containing SST fibers with straight geometric shapes. Consequently, DHST fibers have resulted in a more significant reduction in the workability of the mixtures, leading to higher decreases in the flow diameter (FD) values.
- Compared to the singular usage of SST fibers, the singular utilization of DHST fibers has proven more efficient in improving specimens' physical and mechanical properties against HCL attacks. A primary reason for this efficacy is attributed to the DHST fibers' ability to more effectively restrict the spread of cracks throughout the matrix post-HCL attacks compared to SST fibers. This phenomenon is achieved through the enhanced bridging effect of DHST fibers, which efficiently limits crack propagation within the matrix.
- Micro-SST and macro-DHST fibers elevate RCS and RFS capacities by fortifying specimen integrity post-HCL attacks, curbing the swift and unregulated expansion of micro and macro-sized cracks within the interior network due to their robust adherence with the network.
- Hybrid use of micro-SST and macro-DHST fibers slightly enhances physical and mechanical properties compared to individual fibers. Macro-DHST fibers bridge macro-cracks, while micro-SST fibers prevent micro-crack growth after HCL attacks.
- SEM analysis shows more severe internal damage in specimens exposed to prolonged HCL attacks (28–56 days) compared to shorter exposure (7 days), with hybrid fibers effectively controlling both micro and macro-cracks.
- SF, micro-SST, and macro-DHST fibers improve concrete's resistance to HCL attacks by refining the microstructure, reducing cracks, and limiting crack propagation, enhancing overall durability.

Ethics statement

The manuscript has not been submitted to more than one journal for simultaneous consideration. The submitted work is original and has not been published elsewhere in any form or language.

Disclosure statement

The author has no conflicts of interest to disclose.

Funding

This investigation received financial backing through the FBA-2023-10524 project under the Van Yüzüncü Yıl University BAP Department. Their support was instrumental in facilitating the study's progress and execution.

Data availability statement

The data supporting the findings of this study are available upon reasonable request from the corresponding author.

References

Abbass, W., & Khan, M. I. (2022, August). Experimental and numerical investigation of flexural behavior of hybrid fiber reinforced high strength incorporating a binary and ternary blend of ultra-fines. In *Structures* (vol. 42, pp. 53–64). Elsevier. https://doi.org/10.1016/j.istruc.2022.05.116

Ahmad, S., Al-Amoudi, O. S. B., Khan, S. M., & Maslehuddin, M. (2022). Effect of silica fume inclusion on the strength, shrinkage and durability characteristics of natural pozzolan-based cement concrete. *Case Studies in Construction Materials*, *17*, e01255. https://doi.org/10.1016/j.cscm.2022.e01255

Akarsh, P. K., Marathe, S., & Bhat, A. K. (2021). Influence of graphene oxide on properties of concrete in the presence of silica fumes and M-sand. *Construction and Building Materials*, *268*, 121093. https://doi.org/10.1016/j.conbuildmat.2020.121093

Albattat, R. A., Jamshidzadeh, Z., & Alasadi, A. K. (2020). Assessment of compressive strength and durability of silica fume-based concrete in acidic environment. *Innovative Infrastructure Solutions*, *5*(1), 1–7. https://doi.org/10.1007/s41062-020-0269-1

Ali, B., Kurda, R., Herki, B., Alyousef, R., Mustafa, R., Mohammed, A., Raza, A., Ahmed, H., & Fayyaz Ul-Haq, M. (2020). Effect of varying steel fiber content on strength and permeability characteristics of high strength concrete with micro silica. *Materials*, *13*(24), 5739. https://doi.org/10.3390/ma13245739

Al-Osta, M. A., Sharif, A. M., Ahmad, S., Adekunle, S. K., Al-Huri, M., & Sharif, A. M. (2021). Effect of hybridization of straight and hooked steel fibers and curing methods on the key mechanical properties of UHPC. *Journal of Materials Research and Technology*, *15*, 3222–3239. https://doi.org/10.1016/j.jmrt.2021.10.005

American Society for Testing and Materials ASTM C642. (2013). *Standard Test Method for Density, Absorption, and Voids in Hardened Concrete*. ASTM International.

ASTM C109. (2013). *Standard Test Method for Compressive Strength of Hydraulic Cement Mortars (Using 50 mm Cube Specimens)*. ASTM International.

ASTM C1437. (2015). *Standard Test Method for Flow of Hydraulic Cement Mortar ASTM International*.

ASTM C267. (1997). Standard test methods for chemical resistance of mortars, grouts and monolithic surfacings and polymer concretes. *Annual Book of ASTM Standards Section; ASTM International: West*. 4.

ASTM C348. (2014). *Standard Test Method for Flexural Strength of Hydraulic- Cement Mortars*., ASTM International.

ASTM C597. (2016). *Standard Test Method for Pulse Velocity through Concrete; American Society for Testing and Materials: West*.

ASTM International, ASTM C1585-13. (2013). Standard test method for measurement of the rate of absorption of water by hydraulic-cement concrete.

Bao, X., Li, Y., Chen, X., Yang, H., & Cui, H. (2024). Investigation on the flexural behaviour and crack propagation of hybrid steel fibre reinforced concrete with a low fibre content for tunnel structures. *Construction and Building Materials*, *417*, 135253. https://doi.org/10.1016/j.conbuildmat.2024.135253

Bilal, H., Chen, T., Ren, M., Gao, X., & Su, A. (2021). Influence of silica fume, metakaolin & SBR latex on strength and durability performance of pervious concrete. *Construction and Building Materials*, *275*, 122124. https://doi.org/10.1016/j.conbuildmat.2020.122124

Bin, Y. (2021). Effect of different mineral admixtures on the properties of pervious concrete. *IOP Conference Series: Earth and Environmental Science*, *676*(1), 12070. https://doi.org/10.1088/1755-1315/676/1/012070

Campos, H. F., Klein, N. S., Marques Filho, J., & Bianchini, M. (2020). Low-cement high-strength concrete with partial replacement of Portland cement with stone powder and silica fume designed by particle packing optimization. *Journal of Cleaner Production*, *261*, 121228. https://doi.org/10.1016/j.jclepro.2020.121228

Carrillo, J., Torres, D., & Guerrero, H. (2021). Correlation between results obtained from four-point bending tests (4PBT) and double punch tests (DPT) in concrete reinforced with hooked-end steel fibers. *Engineering Structures*, *239*, 112353. https://doi.org/10.1016/j.engstruct.2021.112353

Chaudhary, S. K., & Sinha, A. K. (2020). Effect of silica fume on permeability and microstructure of high strength concrete. *Civil Engineering Journal*, *6*(9), 1697–1703. https://doi.org/10.28991/cej-2020-03091575

Chen, J., Yuan, Y., Zhu, Q., & Duan, J. (2023). High-temperature resistance of high-strength concrete with iron tailing sand. *Journal of Building Engineering*, *63*, 105544. https://doi.org/10.1016/j.jobe.2022.105544

Das, S. K., Singh, S. K., Mishra, J., & Mustakim, S. M. (2020). Effect of rice husk ash and silica fume as strength-enhancing materials on properties of modern concrete—A comprehensive review. *Emerging Trends in Civil Engineering: Select Proceedings of ICETCE 2018*, 253–266.

Dezhampanah, S., Nikbin, I., Charkhtab, S., Fakhimi, F., Bazkiaei, S. M., & Mohebbi, R. (2020). Environmental performance and durability of concrete incorporating waste tire rubber and steel fiber subjected to acid attack. *Journal of Cleaner Production*, *268*, 122216. https://doi.org/10.1016/j.jclepro.2020.122216

El-Wafa, M. A. (2023). Fiber incorporation and crack control: A synergistic approach to improving serviceability of RC concrete. *Global Journal of Engineering and Technology Advances*, *15*(02), 1–10.

Fattouh, M. S., Tayeh, B. A., Agwa, I. S., & Elsayed, E. K. (2023). Improvement in the flexural behaviour of road pavement slab concrete containing steel fibre and silica fume. *Case Studies in Construction Materials*, *18*, e01720. https://doi.org/10.1016/j.cscm.2022.e01720

Frýbort, A., Štulířová, J., Grošek, J., & Gregerová, M. (2023). Changes in the chemical composition of silica fume in the concrete composite system. *Case Studies in Construction Materials*, *18*, e01916. https://doi.org/10.1016/j.cscm.2023.e01916

Ghaffary, A., & Moustafa, M. A. (2020). Synthesis of repair materials and methods for reinforced concrete and prestressed bridge girders. *Materials*, *13*(18), 4079. https://doi.org/10.3390/ma13184079

Huang, Y., Huang, J., Zhang, W., & Liu, X. (2023). Experimental and numerical study of hooked-end steel fiber-reinforced concrete based on the meso-and macro-models. *Composite Structures*, *309*, 116750. https://doi.org/10.1016/j.compstruct.2023.116750

Huang, Y., Kong, D., Li, Y., Zhou, S., Shu, J., & Wu, B. (2024). Effect of different shapes of steel fibers and palygorskite-nanofibers on performance of ultra-high-performance concrete. *Scientific Reports*, *14*(1), 8224. https://doi.org/10.1038/s41598-024-59020-8

Janowska-Renkas, E., Kaliciak, A., Janus, G., & Kowalska, J. (2021). Durability of cement and ash mortars with fluidized and siliceous fly ashes exposed to HCl acid environment over a period of 2 years. *Materials*, *14*(12), 3229. https://doi.org/10.3390/ma14123229

Jiao, C., Ta, J., Niu, Y., Meng, S., Chen, X. F., He, S., & Ma, R. (2022). Analysis of the flexural properties of ultra-high-performance concrete consisting of hybrid straight steel fibers. *Case Studies in Construction Materials*, *17*, e01153. https://doi.org/10.1016/j.cscm.2022.e01153

Lai, M. H., Wu, K. J., Cheng, X., Ho, J. C. M., Wu, J. P., Chen, J. H., & Zhang, A. J. (2022). Effect of fillers on the behaviour of heavy-weight concrete made by iron sand. *Construction and Building Materials*, *332*, 127357. https://doi.org/10.1016/j.conbuildmat.2022.127357

Li, B., Gao, A., Li, Y., Xiao, H., Chen, N., Xia, D., Wang, S., & Li, C. (2023). Effect of silica fume content on the mechanical strengths, compressive stress–strain behavior and microstructures of geopolymeric recycled aggregate concrete. *Construction and Building Materials*, *384*, 131417. https://doi.org/10.1016/j.conbuildmat.2023.131417

Liu, C., Wang, X., Chen, Y., Zhang, C., Ma, L., Deng, Z., Chen, C., Zhang, Y., Pan, J., & Banthia, N. (2021). Influence of hydroxypropyl methylcellulose and silica fume on stability, rheological properties, and printability of 3D printing foam concrete. *Cement and Concrete Composites*, *122*, 104158. https://doi.org/10.1016/j.cemconcomp.2021.104158

Lv, L. S., Wang, J. Y., Xiao, R. C., Fang, M. S., & Tan, Y. (2021). Influence of steel fiber corrosion on tensile properties and cracking mechanism of ultra-high performance concrete in an electrochemical corrosion environment. *Construction and Building Materials*, *278*, 122338. https://doi.org/10.1016/j.conbuildmat.2021.122338

Ma, X., He, T., Xu, Y., Yang, R., & Sun, Y. (2022). Hydration reaction and compressive strength of small amount of silica fume on cement-fly ash matrix. *Case Studies in Construction Materials*, *16*, e00989. https://doi.org/10.1016/j.cscm.2022.e00989

Madraszewski, S., Sielaff, A. M., & Stephan, D. (2023). Acid attack on concrete—Damage zones of concrete and kinetics of damage in a simulating laboratory test method for wastewater systems. *Construction and Building Materials*, *366*, 130121. https://doi.org/10.1016/j.conbuildmat.2022.130121

Mehta, A., & Ashish, D. K. (2020). Silica fume and waste glass in cement concrete production: A review. *Journal of Building Engineering*, *29*, 100888. https://doi.org/10.1016/j.jobe.2019.100888

Muthu, M., Yang, E. H., & Unluer, C. (2021). Resistance of graphene oxide-modified cement pastes to hydrochloric acid attack. *Construction and Building Materials*, *273*, 121990. https://doi.org/10.1016/j.conbuildmat.2020.121990

Nedunuri, S. S. S. A., Sertse, S. G., & Muhammad, S. (2020). Microstructural study of Portland cement partially replaced with fly ash, ground granulated blast furnace slag and silica fume as determined by pozzolanic activity. *Construction and Building Materials*, *238*, 117561. https://doi.org/10.1016/j.conbuildmat.2019.117561

Paruthi, S., Rahman, I., Husain, A., Hasan, M. A., & Khan, A. H. (2023). Effects of chemicals exposure on the durability of geopolymer concrete ıncorporated with silica fumes and nano-sized silica at varying curing temperatures. *Materials*, *16*(18), 6332. https://doi.org/10.3390/ma16186332

Pather, B., Ekolu, S. O., & Quainoo, H. (2021). Effects of aggregate types on acid corrosion attack upon fly–Ash geopolymer and Portland cement concretes—Comparative study. *Construction and Building Materials*, *313*, 125468. https://doi.org/10.1016/j.conbuildmat.2021.125468

Paul, S. C., van Zijl, G. P., & Šavija, B. (2020). Effect of fibers on durability of concrete: A practical review. *Materials*, *13*(20), 4562. https://doi.org/10.3390/ma13204562

Raju, R. A., Lim, S., Akiyama, M., & Kageyama, T. (2020). Effects of concrete flow on the distribution and orientation of fibers and flexural behavior of steel fiber-reinforced self-compacting concrete beams. *Construction and Building Materials*, *262*, 119963. https://doi.org/10.1016/j.conbuildmat.2020.119963

Ramasamy, S., Shahidan, S., Zuki, S. S., & Azmi, M. A. (2020). A review: Properties of micro steel fibre (MSF) in high-performance concrete in terms of crack propagation. *International Journal of Engineering Trends and Technology*, *68*(11), 113–121. https://doi.org/10.14445/22315381/IJETT-V68I11P215

Ran, B., Omikrine-Metalssi, O., Fen-Chong, T., Dangla, P., & Li, K. (2023). Impact of leaching and chlorides on sulfate attack for cement paste. *Construction and Building Materials*, *376*, 130881. https://doi.org/10.1016/j.conbuildmat.2023.130881

Shariati, M., Shariati, A., Trung, N. T., Shoaei, P., Ameri, F., Bahrami, N., & Zamanabadi, S. N. (2021). Alkali-activated slag (AAS) paste: Correlation between durability and microstructural characteristics. *Construction and Building Materials*, *267*, 120886. https://doi.org/10.1016/j.conbuildmat.2020.120886

Shi, F., Pham, T. M., Tuladhar, R., Deng, Z., Yin, S., & Hao, H. (2023, October). Comparative performance analysis of ground slabs and beams reinforced with macro polypropylene fibre, steel fibre, and steel mesh. In *Structures* (vol. 56, p.104920). Elsevier. https://doi.org/10.1016/j.istruc.2023.104920

Shin, W., & Yoo, D. Y. (2020). Influence of steel fibers corroded through multiple microcracks on the tensile behavior of ultra-high-performance concrete. *Construction and Building Materials*, *259*, 120428. https://doi.org/10.1016/j.conbuildmat.2020.120428

Song, C., Hong, G., & Choi, S. (2020). Effect of dispersibility of carbon nanotubes by silica fume on material properties of cement mortars: Hydration, pore structure, mechanical properties, self-desiccation, and autogenous shrinkage. *Construction and Building Materials*, *265*, 120318. https://doi.org/10.1016/j.conbuildmat.2020.120318

Sposito, R., Maier, M., Beuntner, N., & Thienel, K. C. (2022). Physical and mineralogical properties of calcined common clays as SCM and their impact on flow resistance and demand for superplasticizer. *Cement and Concrete Research*, *154*, 106743. https://doi.org/10.1016/j.cemconres.2022.106743

Taheri, S., Delgado, G. P., Agbaje, O. B., Giri, P., & Clark, S. M. (2020). Corrosion inhibitory effects of mullite in concrete exposed to sulfuric acid attack. *Corrosion and Materials Degradation*, *1*(2), 282–295. https://doi.org/10.3390/cmd1020014

TS EN 196-1. (2009). *Methods of testing cement-Part 1: Determination of strength*. Turkish Standard Institute. [in Turkish].

Wang, J., Dai, Q., Si, R., Ma, Y., & Guo, S. (2020). Fresh and mechanical performance and freeze-thaw durability of steel fiber-reinforced rubber self-compacting concrete (SRSCC). *Journal of Cleaner Production*, *277*, 123180. https://doi.org/10.1016/j.jclepro.2020.123180

Wang, X., Gong, C., Lei, J., Dai, J., Lu, L., & Cheng, X. (2021). Effect of silica fume and nano-silica on hydration behavior and mechanism of high sulfate resistance Portland cement. *Construction and Building Materials*, *279*, 122481. https://doi.org/10.1016/j.conbuildmat.2021.122481

Yoshida, N., & Nakayama, K. (2023). Impact of NaCl on deterioration of hardened cement paste due to sulfuric acid attack. *ce/papers*, *6*(6), 1295–1304. https://doi.org/10.1002/cepa.2997

Youssari, F. Z., Taleb, O., & Benosman, A. S. (2023). Towards understanding the behavior of fiber-reinforced concrete in aggressive environments: Acid attacks and leaching. *Construction and Building Materials*, *368*, 130444. https://doi.org/10.1016/j.conbuildmat.2023.130444

Zeng, W., Ding, Y., Zhang, Y., & Dehn, F. (2020). Effect of steel fiber on the crack permeability evolution and crack surface topography of concrete subjected to freeze-thaw damage. *Cement and Concrete Research*, *138*, 106230. https://doi.org/10.1016/j.cemconres.2020.106230

Zhang, R., Jin, L., & Du, X. (2021). Three-dimensional meso-scale modelling of failure of steel fiber reinforced concrete at room and elevated temperatures. *Construction and Building Materials*, *278*, 122368. https://doi.org/10.1016/j.conbuildmat.2021.122368

Zhang, P., Wang, C., Gao, Z., & Wang, F. (2023). A review on fracture properties of steel fiber reinforced concrete. *Journal of Building Engineering*, *67*, 105975. https://doi.org/10.1016/j.jobe.2023.105975

Zia, A., Zhang, P., & Holly, I. (2023). Long-term performance of concrete reinforced with scrap tire steel fibers in hybrid and non-hybrid forms: Experimental behavior and practical applications. *Construction and Building Materials*, *409*, 134011. https://doi.org/10.1016/j.conbuildmat.2023.134011

Zou, Y. X., Zuo, X. B., Zhang, H. L., & Wang, S. Q. (2023). Influence of fly ash and chlorides on the behavior of sulfate attack in blended cement pastes. *Construction and Building Materials*, *394*, 132231. https://doi.org/10.1016/j.conbuildmat.2023.132231